Modeling Light Trapping in Nanostructured Solar Cells

Vivian E. Ferry,[†,‡,§,*] Albert Polman,[‡] and Harry A. Atwater[†]

[†]Thomas J. Watson Laboratories of Applied Physics, California Institute of Technology, Pasadena, California 91125, United States, and [‡]Center for Nanophotonics, FOM Institute AMOLF, Amsterdam, The Netherlands. [§]Current address: Materials Sciences Division, Lawrence Berkeley National Laboratory and Department of Chemistry, University of California, Berkeley California 94720, United States..

ABSTRACT The integration of nanophotonic and plasmonic structures with solar cells offers the ability to control and confine light in nanoscale dimensions. These nanostructures can be used to couple incident sunlight into both localized and guided modes, enhancing absorption while reducing the quantity of material. Here we use electromagnetic modeling to study the resonances in a solar cell containing both plasmonic metal back contacts and nanostructured semiconductor top contacts, identify the local and guided modes contributing to enhanced absorption, and optimize the design. We then study the role of the different interfaces and show that Al is a viable plasmonic back contact material.

KEYWORDS: thin-film solar cells · surface plasmon · light trapping · photovoltaics · silicon

Light trapping using nanostructures offers one route to cost reduction in photovoltaics. Improved control of light propagation into both localized resonant modes and guided modes allows for enhanced absorption, and thereby photocurrent, while simultaneously reducing the quantity of material utilized.[1] This reduction in solar cell thickness has many potential benefits depending on the semiconductor used, including decreased costs from materials availability, increased manufacturing throughput, increased open circuit voltages, improved carrier collection, and improved stability.[2−4]

A variety of nanoscale methods for light trapping are currently under investigation, including photonic crystals, plasmonic nanostructures, nanowires, and gratings.[5−19] The nanostructures themselves can be metallic, dielectric, or a part of the semiconductor itself.[8,18,20] Likewise, a variety of integration schemes exist, including incorporation of the nanostructures into the contacts or anti-reflection coatings, deposition over existing layers, or embedding within the active region.[21−23] To be effective, the nanostructures must enhance photocurrent across the entire spectral range where the semiconductor is active and be effective at multiple angles of incidence. Additionally, the nanostructures must be compatible with solar cell fabrication processes, low-cost, and offer significant improvements beyond that achievable with existing technologies.

Electromagnetic modeling has become an important tool for optimizing the shape and arrangement of nanostructures for enhanced absorption, and a large number of recent papers explore the enhancements achievable in thin-film Si and other materials systems. A wide variety of simulation and computational techniques have been utilized, including finite element methods, rigorous coupled wave analysis, transfer matrix methods, the discrete dipole approximation, and semiemprical methods.[24−30] These methods differ in the assumptions of symmetry used in the calculations and have varying ability to capture both localized resonances and guided modes. Of course, a complete model would include both optical and electrical components and fully account for carrier collection as well as other cell parameters under different light trapping scenarios.[30] Nevertheless, we show here that optical simulation can compare well to experimental measurements, particularly for extremely thin devices with good carrier collection.

In particular, we use simulation to understand the differences between localized and guided modes in realistic, three-dimensional solar cells and to look at the role of texturing on different interfaces. We have recently fabricated conformal amorphous Si (a-Si:H) solar cells on plasmonic back contacts which show enhanced short-circuit current densities and efficiencies relative to both cells made on flat back contacts and those made on Ag-coated Asahi U-type glass.[9] Ultrathin absorbing layers are particularly important for a-Si:H solar cells for

* Address correspondence to veferry@lbl.gov.

Received for review October 11, 2011 and accepted November 14, 2011.

Published online November 14, 2011
10.1021/nn203906t

long-term stability and manufacturing throughput. In the design discussed in this paper, we use the conformal nature of the deposition to form an integrated device with both plasmonic back contact light trapping and photonic front surface light trapping. Through a combination of local and guided mode resonances, we predict a broad-band response and explore the roles of the different interfaces.

Optical models take the geometry of the system and the optical properties of each material into account, so it is important to model each accurately to compare well to experiment. Given realistic cell depositions, the actual shape of the fabricated device is critical. Here we discuss electromagnetic modeling and optimization of cells using experimental cross sections and atomic force microscopy (AFM) data as a guide to modeling realistic cell architectures. We utilize the finite difference time domain (FDTD) method since finite difference models offer more flexibility than many other simulation methods and do not require assumptions of periodicity or regularity.[31] We include modeling of all necessary spacer layers and optically relevant contacts. The excellent agreement between experimental devices and simulated absorption allows us to both optimize nanostructure designs and understand the mechanisms contributing to light trapping.

RESULTS AND DISCUSSION

We first sought to validate the simulation method against experimentally fabricated devices by using FDTD simulation to directly calculate the generation rate for a given solar cell design.[25,32] The absorption can be calculated from the divergence of the Poynting vector

$$P_{abs} = \frac{1}{2}(\omega\varepsilon''|E|^2 + \omega\mu''|H|^2)$$

where ω is the frequency, ε'' the imaginary part of the permittivity, E is the electric field, μ'' is the imaginary part of the permeability, and H is the magnetic field. For most materials, $\mu'' = 0$ and the second term drops out. The power absorbed can then be converted to photon flux at each wavelength.

$$\Phi(\lambda) = \frac{1}{2\hbar}\varepsilon''|E|^2$$

Since the materials are defined explicitly at every gridpoint, it is straightforward to separate absorption in parasitic materials from absorption in photocurrent-generating materials, even over irregularly shaped features. If the photon flux is integrated over just the photocurrent-generating region and we assume that all power absorbed results in carrier excitation, then this calculates the generation rate $G_{opt}(\lambda)$ in the solar cell at each wavelength. For a final figure of merit, the optical generation rate at each wavelength can be weighted by the power in the solar spectrum in a bin surrounding each point, giving a solar-spectrum-weighted G_{opt}.

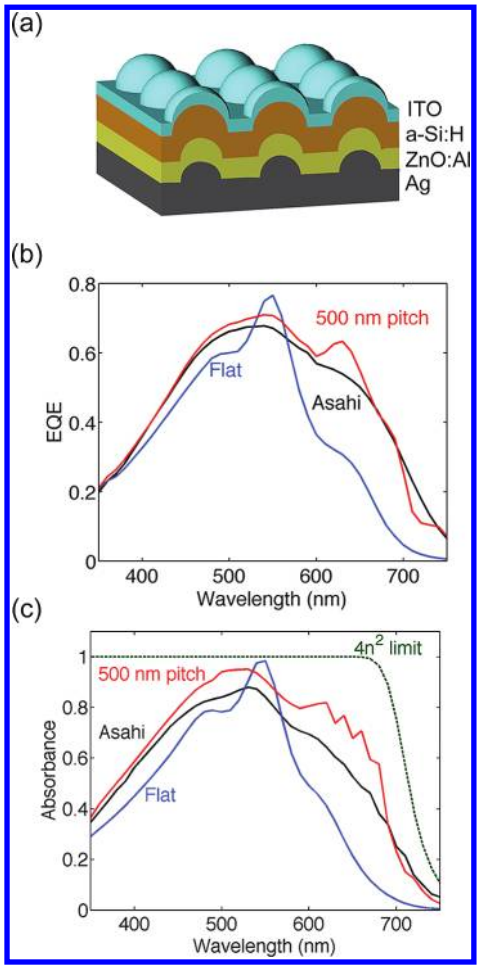

Figure 1. Comparison of simulated absorption to measured external quantum efficiency (EQE). (a) Schematic of general cell design. The ZnO:Al is 130 nm thick, the thickness of the a-Si:H varies, and the ITO is 80 nm thick. Each layer deposits conformally over the preceding layer. (b) Measured EQE spectra for cells with approximately 100 nm *i*-layers with three different surface textures: flat, Ag-coated Asahi glass, and 500 nm pitch nanoparticles as in (a). (c) Calculated absorption in a-Si:H for cells with each of the patterns. The $4n^2$ light trapping limit for this thickness is shown as a reference.

Our general cell design is illustrated in Figure 1a and consists of a patterned metal back contact with 100 nm tall hemiellipsoidal Ag particles on a continuous Ag film, a 130 nm thick layer of ZnO:Al overcoating the Ag, a-Si:H of varying intrinsic layer thickness, and a conformal 80 nm thick layer of indium tin oxide (ITO). The ZnO:Al layer is used in all substrate-type a-Si:H solar cells to prevent diffusion of the Ag into the a-Si:H. The optical properties of the ZnO:Al, a-Si:H, and ITO were taken from spectroscopic ellipsometry measurements. Although the refractive index of a-Si:H can vary throughout the layer and will be different in the doped layers from the intrinsic layer, we neglect those differences and assume the refractive index of a-Si:H is homogeneous. For Ag and the other metals discussed later, we use a Lorentz-Drude fit to Palik's Ag

measurements, following the method of Rakic.[33,34] More details are provided in the Methods section. We chose to use hemiellipsoidal metal nanostructures for a few reasons. First, these hemiellipsoidal shapes avoid the losses associated with nanostructures with high spatial curvature, as discussed elsewhere.[35] Second, these hemiellipsoidal shapes are easily fabricated by methods such as nanoimprint lithography, and the morphology of the complete cells is well-known.[9] By studying details of the light trapping mechanism without varying the shape of the nanostructure, we can be confident that the predictions described here will agree closely with experimental devices.

Figure 1 compares the calculated absorption in a-Si:H to the experimental external quantum efficiency (EQE) for three different geometries. Figure 1b shows the experimental EQE for cells with three different types of nanostructured surfaces: a flat cell, a cell made on Ag-coated Asahi U-type glass, and a cell with 500 nm pitch hemiellipsoidal particles as depicted in Figure 1a, fabricated using nanoimprint lithography. The details of the cell fabrication have been discussed elsewhere.[9,35] The *i*-layer has a thickness of approximately 100 nm. In Figure 1c, we calculated the absorbance for the same set of structures using FDTD. The geometry of each overcoated layer in the periodic case was taken from cross sections of the fabricated devices. For the Asahi textured cells, we imported the profile of the surface directly from AFM data. More details on the simulation setup are given in the Methods section. As a reference, we also show the $4n^2$ light trapping limit for this thickness of a-Si:H.[36] The limit is shown as a metric for comparison of light trapping structures, not as a realistically achievable upper limit for these devices. In particular, this limit is derived for weak absorbers, not for quasi-direct band gap materials such as a-Si:H. Furthermore, in the three simulated cases, as discussed later in the text, a significant fraction of the initial incident power is lost to direct absorption in ITO, which is not captured in the $4n^2$ calculation.

The agreement between experiment and simulation is generally good for all three cases: the leading and falling edges on the blue and red side and the overall spectral shape are very well reproduced by the model. As the simulation technique is only optical and does not account for carrier collection, some features may be magnified in simulation that are not observed as strongly experimentally. Other differences between the two may be due to the assumed geometries or variations in the optical constants, particularly in the a-Si:H layer which varies with the doping and hydrogen content. The agreement between simulation and experiment is generally less accurate on the blue side of the spectrum, which is reasonable considering that the simulation assumes every photon produces one electron, which is collected. At the shorter wavelengths, the collection process is inefficient, and the number of collected electrons will be a lower percentage of the total generated carriers. Nevertheless, the agreement between experiment and simulation in all three cases indicates that simulations are a reasonable and useful tool for optimization of absorption in these solar cells.

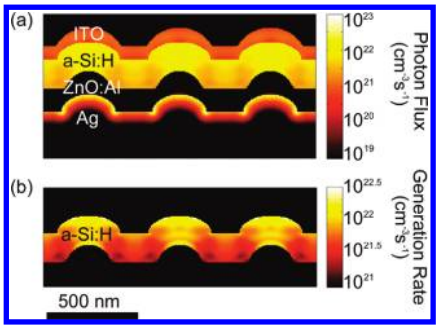

Figure 2. Calculated photon flux and generation rate in the solar cell, weighted by the solar spectrum. The 100 nm tall Ag particles are 300 nm in diameter, the ITO particles are 400 nm in diameter, and the pitch is 500 nm. The *i*-layer thickness is 115 nm. (a) Photon flux showing both the useful photon flux in a-Si:H and the losses in the surrounding materials. (b) Same as (a) but showing only the generation rate in the a-Si:H on a different color scale.

The effect of the light trapping surface on the shape of the EQE and generation rate spectrum is clearly different between these three different cases. The flat cell has a smooth response, with the spectral features determined by thin-film interference. For the periodic cell, sharp peaks are visible on the red side of the spectrum, which we attribute to coupling to waveguide modes.[9] In contrast, the Asahi-patterned cell has a very smooth spectrum due to the randomness of the features. Pseudorandom arrangements of nanoparticles and their effect on the EQE spectrum are discussed elsewhere; here we focus mainly on the design of periodic arrays and the roles of the interfaces.[35]

One of the advantages of this simulation technique is that the fields are calculated explicitly everywhere in the simulation volume. This allows us to visualize the magnitude of the absorption in each of the layers at each wavelength. Figure 2a shows a cross section of the solar-spectrum-weighted generation rate made through one of the simulated periodic cells over the wavelength range from 350 to 800 nm where a-Si:H is active. The color scale is logarithmic. It is evident from the image that absorption is highest in the semiconductor a-Si:H layer, but that absorption in the ITO is also a significant source of loss. The ZnO:Al spacer layer on the back has quite low loss, and the skin depth of the Ag is also visible as absorption here is strongest within the first few nanometers.

We can also examine the profiles of the absorption within the active a-Si:H region for information about the mechanisms leading to enhanced absorption. Figure 2b shows the same data as in Figure 2a, but here the a-Si:H region is isolated and the color scale is modified to show the spatial inhomogeneity of the absorption.

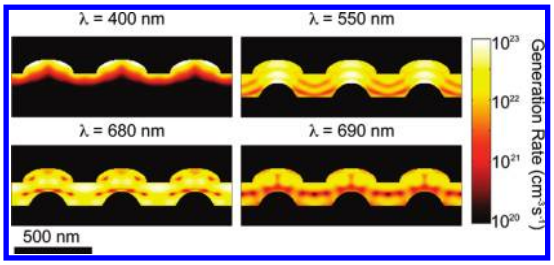

Figure 3. Calculated generation rate maps in a-Si:H at four different wavelengths across the solar spectrum. The pitch and geometry is the same as in Figure 2.

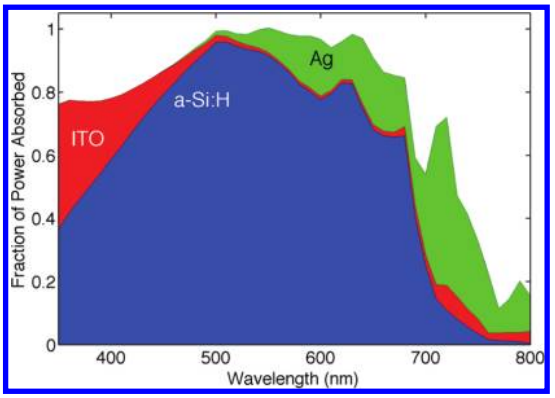

Figure 4. Calculated absorption in each of the layers of the cell. The white area represents light that is lost to reflection. Only absorption in the a-Si:H region contributes to photocurrent, while the absorption in ITO and Ag is parasitic.

The absorption is strongest in the curved region of the cell directly above the scatterer and weaker in the region between the scatterers, indicating that the local absorption effects in these conformal cells can be quite strong.

Figure 3 show maps of the absorption in a-Si:H at four individual wavelengths to investigate the mechanisms that contribute to absorption in different regions of the solar spectrum. In the first panel, the incident wavelength is 400 nm, and it is evident that the absorption is confined to the top portion of the semiconductor. Any enhanced absorption observed or calculated in this spectral range thus cannot be due to the back contact pattern, as the incident light is strongly absorbed before reaching the back. It may, however, result from the front-side curvature of the ITO and a-Si:H. The second panel shows the absorption at $\lambda = 550$ nm, an intermediate wavelength near the thin-film Fabry–Perot resonance for 160 nm thick a-Si:H. A clear standing-wave pattern is observed over the depth of the layer. On the red side of the spectrum, where the propagation lengths in a-Si:H are longer, light couples to waveguide modes with a prominent periodic intensity profile due to scattering from the periode pattern. At $\lambda = 680$ nm, where there is a peak in the calculated photocurrent due to a waveguide mode resonance, the absorption is very strong, whereas at $\lambda = 690$ nm, the mode has been pushed into cutoff and the absorption is much weaker.

The losses in each material are shown quantitatively in Figure 4 as a function of wavelength. As seen in Figure 2, the majority of the absorption is beneficial and occurs in the a-Si:H. On the blue side of the spectrum, from 350 to 500 nm, the parasitic absorption occurs entirely in the ITO layer. This confirms the interpretation that on the blue side the a-Si:H layer is optically thick, and the incident sunlight does not interact with the back metal contact. The non-absorbed fraction is due to reflection. From 500 to 750 nm, the majority of the parasitic absorption is due to the loss in Ag. This loss may be due to the overlap of the waveguide modes with the metal and to the absorption of the nanostructures. To reduce these metal losses, particularly from 500 to 650 nm, we explore the use of other plasmonic metals later in this paper. Finally, we note the sharp peaks in the spectrum attributed to waveguide modes, particularly from 600 to 750 nm. Modification of the nanostructure pitch can tune the spectral position of these modes.[9]

Design and Optimization of Light Trapping Structures. To look in more detail at the role of the waveguide and local modes, we simulated a full range of nanoparticle pitches. Figure 5 shows calculations of the absorption enhancement as a function of pitch for cells with a periodic pattern of hemispherical particles, as in the schematic of Figure 1a. The data are normalized to data for similar cells with Asahi U-type texture. Data are shown as a function of wavelength (a) and integrated over the solar spectrum (b). Two different thicknesses of the cells are used here: 250 nm *i*-layers, to compare to standard a-Si:H solar cells, and ultrathin 115 nm *i*-layers (with 160 nm total a-Si:H thickness). The diameter of the Ag particles and the overcoating parameters are kept fixed, but the pitch between the scatterers is changed; in these simulations, the diameter of the Ag particle is 300 nm and the final ITO particle 400 nm, making 400 nm the closest packed position. We focus on optimizing the arrangement of the particles and their diameter rather than their shape, as the hemiellipsoidal structures used here are easily fabricated by nanoimprint lithography and other methods.[7,9,13]

In Figure 5a, it is evident that scatterers with smaller pitches are broadly more efficient than those with the larger spacings. For small pitch, a broad spectral region of enhancement is observed from $\lambda = 350$ to 650 nm. In the range of $\lambda = 400-500$ nm, a strong onset of high absorption occurs when the wavelength is equal to the pitch, due to the periodicity of the top interface.[37] Several bands of high enhancement are visible in the red portion of the spectrum from 650 to 750 nm, for which the peak enhancement moves to the blue with shorter pitch. We identify these as the Bloch photonic modes of the device, and their positions correspond to the peaks shown in Figure 1. Given the unequal power in the solar spectrum across wavelengths, the pitch

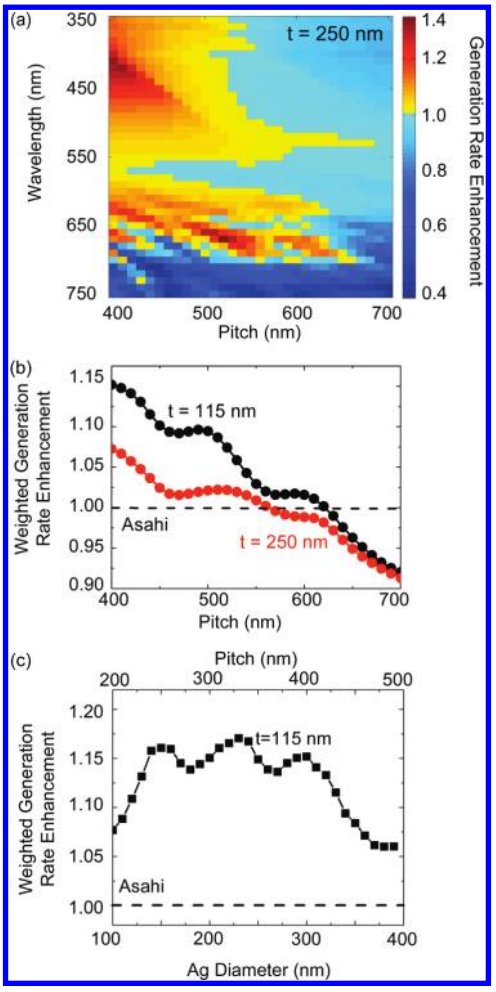

Figure 5. Calculated generation rate enhancements as a function of pitch. The Asahi pattern is a reference in all cases. (a) Enhancement in generation rate as a function of wavelength and pitch for 250 nm thick *i*-layers. (b) Solar-spectrum-weighted generation rate enhancement for cells with 250 nm thick *i*-layers and 115 nm thick *i*-layers. (c) Optimization of pitch and diameter for cells with 115 nm thick *i*-layers. Each pitch is at the closest packed position for the Ag diameter, defined as the point where the overcoated ITO structures are touching without overlapping.

could be designed to result in waveguide modes resonances in an optimal portion of the solar spectrum.[38]

Figure 5b shows the solar-spectrum-weighted absorption, calculated by integrating over each wavelength in Figure 5a. Again, the scale is relative to data for simulated corresponding Asahi cells. Although oscillations are present in Figure 5b, a notable trend is observed: shorter pitches lead to higher integrated absorption. At 400 nm pitch, where the nanostructures are closely packed, a peak enhancement of 7.5% over the randomly textured Asahi cell is observed. For the thinner case shown in Figure 5b, a similar trend is observed, with the largest absorption enhancement also predicted at the closest packed position. For this case, the predicted enhancements are higher, however, with a maximum absorption enhancement of 15% after weighting by the solar spectrum.

The predicted enhancement for closer pitches indicates that the effect of increased absorption depends strongly on the packing fraction of the scatterers. The substantial increase on the blue side of the spectrum must be due to the curvature on the top surface of the cell, not to the structures on the back, as shown in Figure 3. Since the propagation lengths in a-Si:H are short at these wavelengths, increasing the packing fraction for a local effect of the top side curvature will lead to more substantial gains in this region of the spectrum. With careful design, this indicates that both the front and back surfaces can be engineered for an aggregate broad-band response, and that the conformal coating is essential to achieve large absorption enhancements.

Using the packing fraction as a guide, we then optimized the diameter and pitch of a square array for the maximum absorption enhancement. We assume that the closest packed square lattice position for any given Ag diameter produces the high absorption. This assumption has been verified by repeating Figure 5b for other diameters besides the one shown. In Figure 5c, we co-vary the diameter and pitch while keeping maximum packing fraction and plot the enhancement compared to the randomly textured Asahi reference cell. Using Ag as the back contact metal, we predict a maximum absorption enhancement of 17% at a diameter of 230 nm and a pitch of 330 nm.

Role of Front and Back Patterns. One of the issues in understanding the observed light trapping effects is the precise role of the nanostructured metal. The discrete coupling to waveguide modes depends on the periodicity of the metal pattern as is clear from Figure 5a. These waveguide modes that increase photocurrent in the a-Si:H layer are photonic waveguide modes with peak intensity in the a-Si:H layer rather than surface plasmon polariton modes with peak intensity at the Ag/ZnO:Al interface. The effect of the ZnO:Al layer thickness on the waveguide mode structure is shown in Supporting Information Figure 1. The ZnO:Al layer acts as an efficient spacer layer that effectively reduces the coupling to these SPP modes.[39]

The role of the metal nanostructures is thus to provide efficient scattering into waveguide modes, the scattering being efficient due to the high scattering cross section of localized surface plasmon modes of the metal nanostructures. The preferential coupling of scattered light to waveguide modes is a direct consequence of the increased local density of optical states, as shown earlier in, for example, optical microcavities.[40] In addition to being a photonic buffer layer, the ZnO:Al layer serves as a diffusion barrier between the Ag and the a-Si:H during the growth of a-Si:H at elevated temperature, thus reducing unwanted contamination of the semiconductor with Ag, which is known to create carrier recombination traps in a-Si:H.

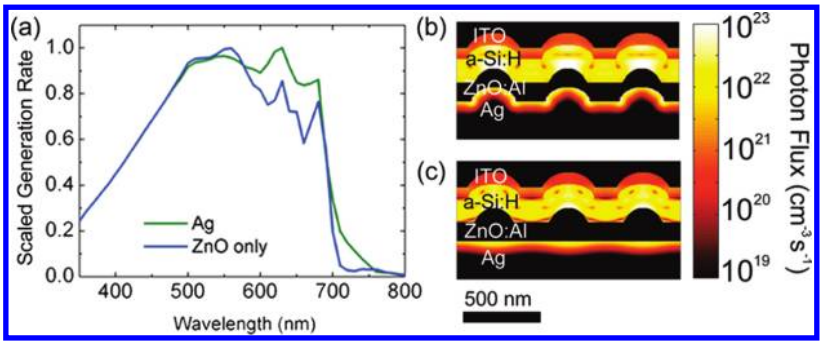

Figure 6. (a) Calculated generation rate for cells with and without plasmonic Ag structures on the back contact. The geometry of the ZnO:Al, a-Si:H, and ITO layers is identical. (b,c) Cross sections of the photon flux at $\lambda = 630$ nm, the wavelength with the greatest difference in the generation rate between the two cases (see a).

To examine the role of the metal, we first analyzed the somewhat unphysical structure shown in Figure 6, where the ZnO:Al is patterned, but the Ag back reflector is assumed to be flat. The volume of the a-Si:H and the geometry of the nanostructures are identical between the two cases. From the calculated generation rate plotted in Figure 6a, we see that many of the spectral features which we attributed to the coupling to waveguide modes occur at the same wavelengths in both cases, but the amplitude of the generation rate from $\lambda = 550$ to 800 nm is strongly reduced for the cells without Ag patterning. This supports the idea that scattering from the metal nanostructure is essential to achieve high photocurrent enhancements. From $\lambda = 350$ to 500 nm the absorption in the two structures is nearly identical, as expected since the only modification is on the back of the device, while light at these wavelengths is fully absorbed in the near-surface region. Figure 6(b) and (c) show cross sections of the generation rate for the two cases at $\lambda = 630$ nm, the wavelength with the largest difference in the two generation rates. Clearly different localized modes are observed for these two structures, with a particularly high absorption enhancement in the a-Si:H around the scatterer for the patterned Ag case. This supports the idea that the high scattering cross section surface plasmon resonance of the metal particle causes increased coupling to the a-Si:H. This example shows the advantage of plasmonic nanostructures over purely dielectric scatterers combined with a back reflector: the presence of the metal leads to higher photocurrent in the semiconductor due to the enhanced scattering cross section of the particle, while parasitic losses in the metal are minimal.

As a second way to probe the role of the metal, we investigated the use of other plasmonic metals as back optical materials. In addition to Ag, we modeled Al, which has a plasmonic resonance at shorter wavelengths, and Au and Cu, which have plasmonic resonances at longer wavelengths than Ag.[25] Figure 7 shows the calculated generation rate spectra for identical structures where the back metal material is

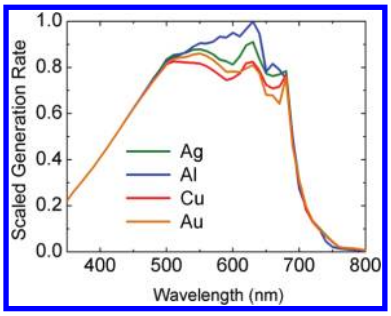

Figure 7. Calculated generation rate for different back contact metals. Each pattern is composed or metal hemispheres of 300 nm diameter with 500 nm pitch, and the overcoating parameters are identical. The a-Si:H *i*-layer is 115 nm thick.

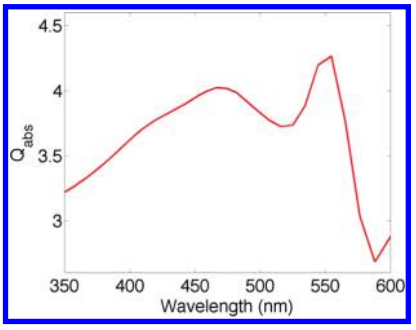

Figure 8. Normalized absorption cross section spectrum for a 350 nm diameter hemiellipsoidal a-Si:H particle with an 80 nm ITO coating on a semi-infinite (nonabsorbing) a-Si:H substrate.

changed. The structure is the same as discussed above: 300 nm diameter particles with 500 nm pitch. As expected, the four metals show identical response from 350 to 500 nm, where light is absorbed in the near-surface region, but the absorption response is quite different from 500 to 700 nm. Interestingly, while many of the spectral features occur at the same wavelengths, as expected because the waveguide modes in the a-Si:H are identical, the absorption in the a-Si:H is much higher when Al is used as the back contact rather than Ag. We attribute this effect to the reduced absorption cross section of the Al nanoparticles relative

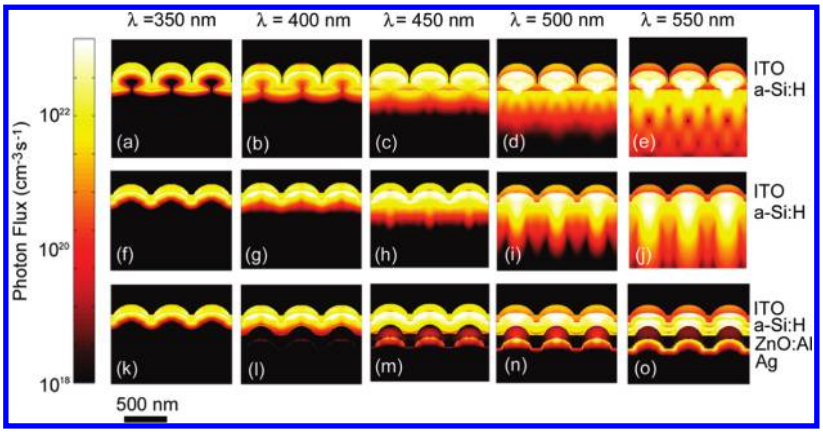

Figure 9. Photon fluxes at several wavelengths to look at the role of the top-side structures. (a−e) Ellipsoidal a-Si:H particles coated with ITO on a semi-infinite a-Si:H substrate. (f−j) Hemiellipsoidal a-Si:H particles coated with ITO, showing much stronger interaction with the substrate. (k−o) Thin-film configuration with a 90 nm a-Si:H i-layer.

to Ag when coupled to the metallic substrate. Particle−substrate coupling effects are known to strongly influence the position of resonance for nanostructures.[41] From calculations of the cross sections, we find that the absorption cross section for the Al particles is lower across the spectral range from 520 to 720 nm than for Ag, leading to fewer parasitic losses. The absorption cross section is somewhat higher than Ag from λ = 350−520 nm and from λ = 720−800 nm, consistent with the data shown in Figure 7. Since these particles are on the back of cell, light in the λ = 350−520 nm range is primarily absorbed in the cell before interacting with the back contact. From λ = 720−800 nm, the absorption in a-Si:H is weak, resulting in minimal effect on the overall calculated photocurrent. The scattering cross section for Al is also somewhat reduced relative to Ag, but it is sufficiently high to enable good coupling to the waveguide modes.

We now turn our attention to the role of the top interface. On the blue side of the spectrum, we predict and experimentally observe a significant enhancement in absorption (see Figure 5).[35] Since cells of 115 nm *i*-layer thickness are optically thick at these wavelengths, this enhanced photocurrent can only be due to the top-side a-Si:H/ITO nanostructuring. As each successive layer deposits conformally over the back Ag particles, the top interface can be described as a-Si:H hemiellipsoids with an ITO coating.

Spherical (or hemispherical) scatterers can have scattering and absorption cross sections several times their geometrical cross section.[20] The figure of merit for these resonant absorbers is the normalized absorption cross section Q_{abs}, defined as the ratio between absorption and geometrical cross section

$$Q_{abs} = \frac{\sigma_{abs}}{\sigma_{geom}}$$

Figure 8 shows a calculation of Q_{abs} for a 350 nm diameter a-Si:H hemiellipsoid with an 80 nm ITO coating, which corresponds to the experimental parameters on a semi-infinite a-Si:H substrate. The absorption in the substrate is set to zero to separate the effect of absorption in the particle from transmission into the substrate. The figure shows two clear absorption resonances with a peak value of Q_{abs} near 4. The resonance line width is larger for the lowest wavelength resonance, which is due to the stronger absorption in the a-Si:H at shorter wavelengths. Figure 8 shows that incident light interacts strongly with these surface nanoscatterers over a broad spectral range from λ = 350−550 nm. This is consistent with the broad absorption enhancement in the blue observed in the simulations in Figure 5.

Hemiellipsoidal particles have similar resonances to their ellipsoidal counterparts but interact more strongly with the substrate. To illustrate this, Figure 9 shows calculations of the calculated photon flux for three different structures across the spectral range from λ = 350−550 nm. The top row shows the photon flux profile for an ITO-coated array of a-Si:H ellipsoids on a semi-infinite a-Si:H substrate, the middle row shows the hemiellipsoidal structure on a semi-infinite a-Si:H substrate, and the third row shows the full cell layout including the Ag and ZnO:Al layers and an a-Si:H *i*-layer thickness of 90 nm. The substrate is absorbing in these simulations, the Ag particle diameter is 300 nm, and the array pitch is 400 nm. Comparing the first and second rows, it is evident that the ellipsoid (a−e) has stronger resonant absorption inside the particle than the hemiellipsoid (f−j), with weaker coupling into the substrate for the ellipsoid. At λ = 550 nm, on the absorption resonance in Figure 8, the ellipsoid has a weak scattering intensity profile into the substrate, whereas the hemiellipsoid shows a more intense intensity profile extending into the substrate. This is the wavelength of the narrow resonance seen in Figure 8. For solar cell applications, the coupling of power into the substrate is more advantageous for enhancing photocurrent. Absorption confined within the ellipsoids will be difficult to collect, but with hemiellipsoidal

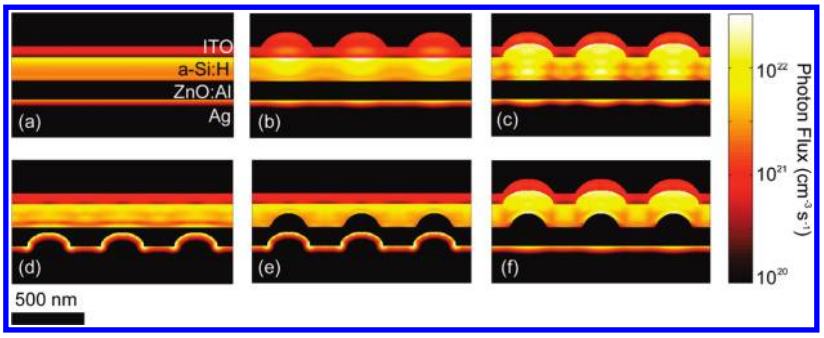

Figure 10. Solar-spectrum-weighted photon flux for several different permutations of the cell geometry. The highest overall absorption occurs for a structure with patterned front and back surfaces.

particles, the resonant absorption can be redirected into the substrate. Similar resonances are observed in the realistic thin-film cases (k–o).

The strong resonant absorption of these semiconductor–dielectric nanostructures demonstrates that front and back-side textures can be utilized in combination with plasmonic nanostructures to enable broadband photocurrent enhancement. The semiconductor resonances could be tuned to the blue side of the spectrum, while the back-side metal patterns are designed for coupling into waveguide modes on the red side of the spectrum. The semiconductor structures could also be used alone for enhancing light absorption in structures where the back metal surface cannot be easily structured.

Figure 10 shows the distinctive absorption profiles from a series of different permutations on the original structure, with front and/or back interfaces patterned with arrays of hemiellipsoids.[42] Figure 10a shows the generation rate profiles weighted over the solar spectrum for an unpatterned cell for reference. Figure 10b,c shows top-side patterns of either exclusively ITO or a-Si:H/ITO. The absorption in both of these cases is predominantly localized underneath the scatterers, as discussed above. The purely dielectric, ITO-only case (Figure 10b) shows somewhat lower absorption but is promising as it does not involve structuring the semiconductor, which could be used in cases where the properties of the semiconductor prohibit direct texturing. Figure 10d,e shows back-side only patterns, where either only the Ag or the Ag and ZnO:Al are patterned. Here the absorption profile is more spread out, reflecting the coupling to waveguide modes. Finally, Figure 10f shows the same structure discussed in Figure 7, where the Ag is flat but all of the other interfaces are patterned. This shows clearly stronger absorption than any of the preceding cases. Including both the front and back surface patterns thus allows for a combination of localized and waveguide modes in the device, leading to the strongest broad-band absorption enhancement.

CONCLUSIONS

In the drive to reduce the cost of photovoltaics, light trapping has emerged as a method to employ ultrathin semiconductor volumes while maintaining high efficiencies. With the implementation of techniques such as nanoimprint lithography, these patterns can be fabricated over large areas inexpensively. Likewise, electromagnetic simulation has emerged as a critical and viable tool for optimizing the design of structures, with the capability to model periodic, quasi-periodic, and randomly textured surfaces with good fidelity.

Our design takes advantage of realistic conformal deposition conditions to design a device with broadband absorption enhancement based on several different resonances. Localized resonances within the semiconductor play a key role in enhancing absorption on the blue side of the spectrum. The metal patterns on the back contact are then used to couple red light into waveguide modes of the cell. Through simulation of the different permutations, we identify the roles of each of the interfaces in light trapping. An ideal light trapping geometry is composed of separately optimized front and back nanopatterns. Finally, we show that Al is a viable back contact material in these designs, with the potential for higher photocurrents than Ag.

METHODS

All simulations were performed using Lumerical FDTD simulation software. The optical data for ITO, a-Si:H, and ZnO:Al were taken from spectroscopic ellipsometry measurements. For Ag, we used a Lorentz–Drude fit to data from Palik, using tabulated literature values for the Lorentz–Drude parameters.[34] We imported the data to the software with very fine wavelength steps to avoid fitting errors from the simulation package.

For the nanopatterned cells, the overcoating parameters were taken from cross sections through the fabricated cells. For Ag particles of 300 nm diameter, we assumed that the ZnO:Al broadened to 325 nm, the a-Si:H particle to 375 nm, and the ITO to 400 nm. For the Asahi cells, we imported AFM data measured on Ag-coated Asahi substrates. Rather than making assumptions about broadening after deposition, the same texture was used through each layer. The Asahi patterns were

simulated over a 2 μm $\times$ 2 μm region with periodic boundary conditions. While this periodic assumption could introduce errors, the standard deviation of the generation rate was estimated using a statistical bootstrapping method and verified to be less than 5% at all wavelengths. Simulations of other regions on the same substrate also showed similar generation rates.

Acknowledgment. We are grateful to R. Schropp, C. van der Werf, and M. Verschuuren for cell fabrication. The Caltech portion of this work was supported by the Department of Energy under Contract Number DE-FG02-07ER46405 (modeling) and SETP GO-18006 (cell fabrication). Work at AMOLF is part of the research program of FOM which is financially supported by NWO; it is also supported by the European Research Counsel. This work is also part of the Global Climate and Energy Project (GCEP).

Supporting Information Available: Dispersion relations showing the effect of ZnO:Al layer thickness on the waveguide modes of the cell structure. This material is available free of charge *via* the Internet at http://pubs.acs.org.

REFERENCES AND NOTES

1. Atwater, H. A.; Polman, A. Plasmonics for Improved Photovoltaic Devices. *Nat. Mater.* **2010**, *9*, 205–213.
2. Shah, A. V.; Schade, H.; Vanecek, M.; Meier, J.; Vallat-Sauvain, E.; Wyrsch, N.; Kroll, U.; Droz, C.; Bailat, J. Thin-Film Silicon Solar Cell Technology. *Prog. Photovoltaics* **2004**, *12*, 113.
3. Staebler, D. L.; Wronski, C. R. Reversible Conductivity Changes in Discharge-Produced Amorphous Silicon. *Appl. Phys. Lett.* **1977**, *31*, 29.
4. Campbell, P.; Green, M. A. The Limiting Efficiency of Silicon Solar-Cells under Concentrated Sunlight. *IEEE Trans. Electron Devices* **1986**, *33*, 2934–239.
5. Mallick, S. B.; Agrawal, M.; Peumans, P. Optimal Light Trapping in Ultra-thin Photonic Crystal Crystalline Silicon Solar Cells. *Opt. Express* **2010**, *18*, 5691–5706.
6. Mutitu, J. G.; Shi, S.; Chen, C.; Creazzo, T.; Barnett, A.; Honsberg, C.; Prather, D. W. Thin Film Silicon Solar Cell Design Based on Photonic Crystal and Diffractive Grating Structures. *Opt. Express* **2008**, *16*, 15238–15248.
7. Zhu, J.; Hsu, C.-M.; Yu, Z.; Fan, S.; Cui, Y. Nanodome Solar Cells with Efficient Light Management and Self-Cleaning. *Nano Lett.* **2010**, *10*, 455–459.
8. Naughton, M. J.; Kempa, K.; Ren, Z. F.; Gao, Y.; Rybczynski, J.; Argenti, N.; Gao, W.; Wang, Y.; Peng, Y.; Naughton, J. R.; *et al.* Efficient Nanocoax-Based Solar Cells. *Phys. Status Solidi RRL* **2010**, *4*, 181–183.
9. Ferry, V. E.; Verschuuren, M. A.; Li, H. B. T.; Verhagen, E.; Walters, R. J.; Schropp, R. E. I.; Atwater, H. A.; Polman, A. Light Trapping In Ultrathin Plasmonic Solar Cells. *Opt. Express* **2010**, *18*, A237–A245.
10. Eisele, C.; Nebel, C. E.; Stutzmann, M. Periodic Light Coupler Gratings in Amorphous Thin Film Solar Cells. *J. Appl. Phys.* **2001**, *89*, 7722.
11. Haase, C.; Stiebig, H. Thin-Film Silicon Solar Cells with Efficient Periodic Light Trapping Texture. *Appl. Phys. Lett.* **2007**, *91*, 061116.
12. Müller, J.; Rech, B.; Springer, J.; Vanecek, M. TCO and Light Trapping in Silicon Thin Film Solar Cells. *Solar Energy* **2004**, *77*, 917–930.
13. Shir, D.; Yoon, J.; Chanda, D.; Ryu, J. H.; Rogers, J. A. Performance of Ultrathin Silicon Solar Microcells with Nanostructures of Relief Formed by Soft Imprint Lithography for Broad Band Absorption Enhancement. *Nano Lett.* **2010**, *10*, 3041–3046.
14. Biswas, R.; Xu, C. Nano-Crystalline Silicon Solar Cell Architecture with Absorption at the Classical $4n^2$ Limit. *Opt. Express* **2011**, *19*, A664–A672.
15. Hägglund, C.; Kasemo, B. Nanoparticle Plasmonics for 2D-Photovoltaics: Mechanisms, Optimization, and Limits. *Opt. Express* **2009**, *17*, 11944–11957.
16. Munday, J. N.; Atwater, H. A. Large Integrated Absorption Enhancement in Plasmonic Solar Cells by Combining Metallic Gratings and Antireflection Coatings. *Nano Lett.* **2011**, *11*, 2195–2201.
17. Wang, W.; Wu, S.; Reinhardt, K.; Lu, Y.; Chen, S. Broadband Light Absorption Enhancement in Thin-Film Silicon Solar Cells. *Nano Lett.* **2010**, *10*, 2012–2018.
18. Grandidier, J.; Callahan, D.; Munday, J. N.; Atwater, H. A. Light Absorption Enhancement in Thin-Film Solar Cells Using Whispering Gallery Modes in Dielectric Nanospheres. *Adv. Mater.* **2011**, *23*, 1272.
19. Lee, B. G.; Stradins, P.; Young, D. L.; Alberi, K.; Chuang, T.-K.; Couillard, J. G.; Branz, H. M. Light Trapping by a Dielectric Nanoparticle Back Reflector in Film Silicon Solar Cells. *Appl. Phys. Lett.* **2011**, *99*, 064101.
20. Cao, L.; White, J. S.; Park, J.-S.; Schuller, J. A.; Clemens, B. M.; Brongersma, M. L. Engineering Light Absorption in Semiconductor Nanowire Devices. *Nat. Mater.* **2009**, *8*, 643–647.
21. Lee, J.-Y.; Peumans, P. The Origin of Enhanced Optical Absorption in Solar Cells with Metal Nanoparticles Embedded in the Active Layer. *Opt. Express* **2010**, *18*, 10078–10087.
22. Spinelli, P.; Hebbink, M.; de Waele, R.; Black, L.; Lenzmann, F.; Polman, A. Optical Impedance Matching Using Coupled Plasmonic Nanoparticle Arrays. *Nano Lett.* **2011**, *11*, 1760–1765.
23. Catrysse, P. B.; Fan, S. Nanopatterned Metallic Films for Use as Transparent Conductive Electrodes in Optoelectronic Devices. *Nano Lett.* **2010**, *10*, 2944–2949.
24. Rockstuhl, C.; Fahr, S.; Bittkau, K.; Beckers, T.; Carius, R.; Haug, F.-J.; Söderström, T.; Ballif, C.; Lederer, F. Comparison and Optimization of Randomly Textured Surfaces in Thin-Film Solar Cells. *Opt. Express* **2010**, *18*, A335–A342.
25. Ferry, V. E.; Munday, J. N.; Atwater, H. A. Design Principles for Plasmonic Photovoltaics. *Adv. Mater.* **2010**, *22*, 4795–4808.
26. Zeman, M.; van Swaaij, R. A. C. M. M.; Metselaar, J. W.; Schropp, R. E. I. Optical Modeling of a-Si:H Solar Cells with Rough Interfaces: Effect of Back Contact and Surface Roughness. *J. Appl. Phys.* **2000**, *88*, 6436–6443.
27. Catchpole, K. R.; Pillai, S. Absorption Enhancement Due to Scattering by Dipoles into Silicon Waveguides. *J. Appl. Phys.* **2006**, *100*, 044504.
28. Rockstuhl, C.; Fahr, S.; Lederer, F.; Bittkau, K.; Beckers, T.; Carius, R. Local *versus* Global Absorption in Thin-Film Solar Cells with Randomly Textured Surfaces. *Appl. Phys. Lett.* **2008**, *93*, 061105.
29. Lin, A.; Phillips, J. Optimization of Random Diffraction Gratings in Thin-Film Solar Cells Using Genetic Algorithms. *Sol. Energy Mater. Sol. Cells* **2008**, *92*, 1689–1696.
30. Li, X.; Hylton, N. P.; Giannini, V.; Lee, K.-H.; Ekins-Daukes, N. J.; Maier, S. A. Bridging Electromagnetic and Carrier Transport Calculations for Three-Dimensional Modeling of Plasmonic Solar Cells. *Opt. Express* **2011**, *19*, A888–A896.
31. Taflove, A.; Hagness, S. C. *Computational Electrodynamics: The Finite Difference Time-Domain Method*; Artech House: Norwood, MA, 2000.
32. Yaghjian, A. D. Internal Energy, Q-Energy, Poynting's Theorem, and the Stress Dyadic in Dispersive Material. *IEEE Trans. Antennas Propagations* **2007**, *55*, 1495–1505.
33. Palik, E.; Ghosh, G. *Handbook of Optical Constants of Solids*; Academic Press: New York, 1997; Vol. 3.
34. Rakic, A. D.; Djurisic, A. B.; Elazar, J. M.; Majewski, M. L. Optics Properties of Metallic Films for Vertical-Cavity Optoelectronic Devices. *Appl. Opt.* **1998**, *37*, 5271–5283.
35. Ferry, V. E.; Verschuuren, M. A.; van Lare, M. C.; Schropp, R. E. I.; Atwater, H. A.; Polman, A. Optimized Spatial Correlations for Broadband Light Trapping Nanostructures in High-Efficiency Ultra-thin Film a-Si:H Solar Cells. *Nano Lett.* **2011**, *11*, 4239–4245.
36. Yablonovitch, E. Statistical Ray Optics. *J. Opt. Soc. A* **1982**, *72*, 899–907.
37. Huang, Y.-F.; Chattopadhyay, S.; Jen, Y.-J.; Peng, C.-Y.; Liu, T.-A.; Hsu, Y.-K.; Pan, C.-L.; Lo, H.-C.; Hsu, C.-H.; Chang, Y.-H.; *et al.* Improved Broadband and Quasi-Omnidirectional Anti-reflection Properties with Biomimetic Silicon Nanostructures. *Nat. Nanotechnol.* **2007**, *2*, 770–774.

38. Saeta, P. N.; Ferry, V. E.; Pacifici, D.; Munday, J. N.; Atwater, H. A. How Much Can Guided Modes Enhance Absorption in Thin Solar Cells? *Opt. Express* **2009**, *17*, 20975–20990.
39. Haug, F.-J.; Söderström, T.; Cubero, O.; Terrazoni-Daudrix, V.; Ballif, C. Influences of the ZnO Layer Structure on the Guided Mode Structure in Si/ZnO/Ag Multilayers. *J. Appl. Phys.* **2009**, *106*, 044502.
40. Kippenberg, T. J.; Tchebotareva, A. L.; Kalkman, J.; Polman, A.; Vahala, K. J. Purcell-Factor-Enhanced Scattering from Si Nanocrystals in an Optical Microcavity. *Phys. Rev. Lett.* **2009**, *103*, 027406.
41. Halas, N. J.; Lal, S.; Chang, W.-S.; Link, S.; Nordlander, P. Plasmons in Strongly Coupled Metallic Nanostructures. *Chem. Rev.* **2011**, *111*, 3913–3961.
42. Sai, H.; Jia, H.; Kondo, M. Impact of Front and Rear Texture of Thin-Film Microcrystalline Silicon Solar Cells on Their Light Trapping Properties. *J. Appl. Phys.* **2010**, *108*, 045505.